Breathing mode of nanoclusters: Definition and comparison to a continuous medium model

B. Lan and D. Y. Sun

Department of Physics, East China Normal University, Shanghai 200062, China

Breathing modes are closely related to many physical properties of nanoclusters. Decades of research, however, failed to formulate a general and unambiguous definition. Here we present a straightforward and widely applicable definition of breathing modes based on power spectra of geometric quantities, namely, surface area, volume, etc. Applying group theory, normal-mode analysis, and molecular dynamics simulations, we have explored breathing modes of several Al_n clusters with high and low symmetries. The results suggest that our definition is able to cover not only common breathing modes but also some *hidden* modes. Our consistent definition also allows us to make a comprehensive and in-depth comparison with Lamb's continuous medium model, which reveals some high-frequency breathing modes are explicable only at the atomic level.

I. INTRODUCTION

Vibrational properties provide essential insights into the nature of nanoclusters and serve as a unique characterization for morphology [1], thermodynamic quantities [2,3], surface effects [1,4], etc. Among normal modes, the so-called breathing modes (BMs), simple and experimentally detectable, are of fundamental interest.

BMs are usually considered a type of vibration which induces expansion and contraction of a finite system. This phenomenological picture of BMs, however, creates ambiguity and inconsistency. For instance, BMs have been defined as *uniform* modes [5–9], namely, in-phase or equal-amplitude vibrations. The latter imposes an extremely stringent condition on nanoclusters, which requires all atomic sites except the body center to be equivalent. In fact, for realistic systems, only a few nanoclusters fulfill such a prerequisite. Considering the facts mentioned above, most studies focused on radial breathing modes (RBMs) [10–13]. The analytical theory for RBMs in trapped systems formulated by Olivetti *et al.* [14] may be the one capable of capturing some universal features. To the best of our knowledge, out-of-phase BMs, such as axial ones (ABMs, also known as quadrupolar modes), are less studied [15]. Suppose we approximate nanoclusters to a continuous elastic sphere belonging to the full $O(3)$ rotation group; both radial ($D_g^{(0)}$) and axial ($D_g^{(2)}$) breathing (Fig. 1) are Raman active and thus experimentally non-negligible. What is more, for low-symmetry nanoclusters, due to their asymmetric normal modes, it is quite a challenge to define a reasonable BM coinciding with the phenomenological description.

Considering the incompleteness of the definition for BMs, Henning *et al.* suggested a solution by defining quasi-BMs, in which some of the smallest deviations from uniform BMs are taken as a criterion [16]. However, the "smallest deviation" still contains considerable ambiguity and may be far from enough to encapsulate all cases. The projection approach adopted by several authors [1,16–18] could exclude out-of-phase BMs in some circumstances and could

also be problematic for degenerate ABMs (see Ref. [17] and Sec. III A).

Apart from atomic models, Lamb studied BMs of an isotropic sphere based on the continuous elastic theory (CET) [19,20]. He classified vibrational modes into two types: (i) torsional modes that preserve the density and (ii) spherical modes that usually induce volume oscillations [21]. As discussed above, we are concerned with only two spherical modes with angular momenta $l = 0$ and $l = 2$, analogous to radial and axial breathing, respectively. Lamb's results show that frequencies of spherical modes are proportional to the reciprocal of sphere diameters [19,22]. Among many nanoclusters [1,3,18,23–25], this linear relationship is found to be valid for the lowest-frequency BMs, even for clusters containing only a few atoms. Naturally, one may ask when a CET would break down. The question still remains open.

In this paper, we present a precise, semiphenomenological definition for BMs. Applying group theory and numerical calculations, we demonstrate that our definition is able to cover not only common BMs but also some *hidden* modes. By comparing our results with Lamb's continuous medium model, we find that some high-frequency BMs can be explained only at the atomic level.

II. METHOD

Information about BMs is encoded in the power spectra (PS) of fluctuations in geometrical quantities [GQs, denoted $Q(t)$]. Then we have

$$\Delta Q(t) = Q(t) - \langle Q(t) \rangle, \tag{1}$$

$$\mathrm{PS} = \mathcal{F}(\langle \Delta Q(0) \Delta Q(t) \rangle). \tag{2}$$

Here $\langle \cdot \rangle$ is a time average, $\Delta Q(0)\Delta Q(t)$ is the time autocorrelation function of $\Delta Q(t)$, and $\mathcal{F}$ denotes a Fourier transform. PS can easily be obtained from molecular dynamics (MD) simulations. By appropriately choosing $Q(t)$ (see below), peaks in PS would indicate only RBMs and/or ABMs.
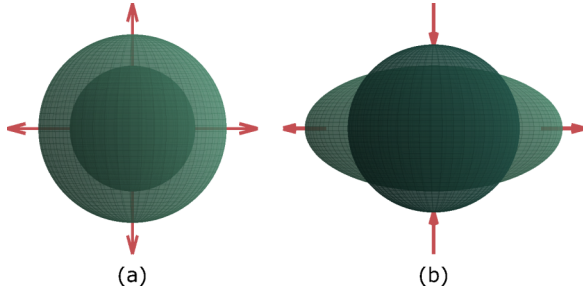
FIG. 1. Illustrations of (a) radial and (b) axial breathing modes of an ideal elastic sphere. A monopolar RBM executes isotropic expansion and contraction, while under a quadrupolar ABM it oscillates between an oblate and prolate spheroid along an axis. At the atomic level, symmetry decreases, and uncertainty arises, and normal modes may not coincide with macroscopic vibrational modes. This poses a challenge to precisely define BMs for nanoclusters, especially for *amorphous* clusters.

Consequently, we define a BM as the mode with *obvious* peaks in PS. Obviousness here refers to some conventional peak-detecting technique, for example, a relative or absolute threshold above background noises. The choice depends on practical contexts and intentions. We will soon see that, with certain well-defined $Q(t)$, this semiphenomenological definition is straightforward and consistent. If $Q(t)$ is properly chosen, the above definition is applicable to any system at *finite* temperatures, even without calculating displacements or inspecting symmetry.

Similar techniques have been applied to pinpoint RBMs of carbon nanotubes [26–28] (note that RBMs for a cylindrically symmetric system are not the same as those of spherical bodies). In this work, we try to extend this approach to more general circumstances and examine the underlying physics.

For RBMs, characteristic GQs could be volume V and surface area S. Because of inherent uncertainty in GQs of finite systems, we chose three different algorithms. One is the ellipsoidal approximation (labeled V_e, S_e); another is based on convex bounding (denoted by V_h, S_h). Volume is also calculated as a sum of approximated Wigner-Seitz cells (marked V_{ws}). Explicit formulas of V_e and S_e read [29]

$$V_e = \frac{4}{3}\pi R_a R_b R_c, \tag{3}$$

$$S_e = 2\pi R_c^2 + \frac{2\pi R_a R_b}{\sin(\phi)}[E(\phi, k)\sin^2(\phi)$$
$$+ F(\phi, k)\cos^2(\phi)], \quad R_a > R_b > R_c, \tag{4}$$

where R_a, R_b, and R_c are radii of gyration and $E(\phi, k)$ and $F(\phi, k)$ are incomplete elliptic integrals. V_h and S_h are defined as the total volume of tetrahedra and the total area of surface Delaunay triangles [30], respectively. V_{ws} can be calculated as

$$V_{ws} = \sum_{i=1}^{N} v_i, \tag{5}$$

$$v_i = \gamma_i \frac{4\pi}{3} \sum_{j}' \left(\frac{r_{ij}}{2}\right)^3. \tag{6}$$

$\sum'$ includes only the nearest neighbors within a cutoff distance $r_c^{(ws)}$; γ_i is a constant or some smooth real function. For details on V_{ws}, see Refs. [31,32].

Each GQ presented above reflects some specific aspects of shape distortion. They can be classified into two categories: (i) V_e and S_e mainly depend on the rms radius (RMSR, $\mathscr{R}$) of a nanocluster,

$$\mathscr{R} = \sqrt{\frac{\sum_{i=1}^{N} r_i^2}{N}}, \tag{7}$$

$$V_e \sim O(\mathscr{R}^3), \tag{8}$$

$$S_e \sim O(\mathscr{R}^2). \tag{9}$$

(ii) V_h, S_h, and V_{ws} relate to pair distances $\{r_{ij}\}$. Note that S_h and V_h depend only on surface atoms, but S_e and V_{ws}, without this feature, are less sensitive to surface waves. Similarly, V_e is insusceptible to *local* rearrangements. For some BMs, fluctuations in V_h are subtler than that of S_h, such as those modes where the average density is nearly unchanged. This, of course, does not ensure the cluster acts like an incompressible elastic body since it may be subject to *internal* contraction.

For ABMs, radii of gyration (R_α) and flattening ($e_{\alpha\beta} = |R_\alpha - R_\beta|/R_\alpha$) are reasonable and well-defined GQs. The square root in eccentricity will increase round-off errors; thus, we use flattening instead. Empirical studies show that errors induced by subtracting two similar radii (i.e., $|R_\alpha - R_\beta|$) are endurable. An issue arises when isotropic RBMs appear in PS of R_α, which can be alleviated by comparing with RBM signals. From this aspect, $e_{\alpha\beta}$ is much better since no isotropic mode can emerge in the radii difference $|R_\alpha - R_\beta|$.

In MD simulations for finite systems, in order to maintain the correct temperature, it is necessary to exclude the global translation and rotation. However, some numerical methods would generate tiny rotatory drifts even though the net total angular momentum is subtracted periodically. Such tiny rotatory drifts are observable only in a sufficiently long run. Their effects on the breathing mode are thus ignorable as the major contributions in power spectra are short-time correlations. Without suppressing rotary effects, a simple trick is to sort R_α by length. Sorted values are denoted by $R_\alpha^{(s)}$ and $e_{\alpha\beta}^{(s)}$.

All GQs are *instantaneous* quantities. The monopolar nature of RBMs necessitates a change in surface areas of a cluster, whereas isotropic movements cancel differences between R_α so that $e_{\alpha\beta}$ remains constant. Since ABMs are anisotropic, both R_α and $e_{\alpha\beta}$ undergo observable changes.

With GQs defined above, we performed constant-energy MD simulations to calculate PS and identify BMs. The MD time step is 1 fs, and the system is equilibrated at 100 K. Newtonian equations of motion are integrated with the Nordsieck predictor-corrector algorithm [33,34]. The system first is allowed to equilibrate up to a few nanoseconds and is then simulated for a few more nanoseconds; PS are calculated from MD trajectories.

As an illustration and verification, we calculated BMs of several Al_n. Three Mackay icosahedral clusters (Al_{13}, Al_{55}, and Al_{147}, I_h point group) and a disordered Al_{43} (C_s point group) are chosen. Configurations of these clusters are available in the Cambridge Cluster Database [35]. The interatomic potential is modeled by a highly transferable glue potential

TABLE I. Breathing modes of I_h and C_s clusters.

Point group	Type[a]	Irrep[b]	Angular momentum	Degeneracy	Raman[c]	Infrared[c]	Lamb mode[d]	Irrep of $O(3)$[b]
I_h	RBM	A_g	$l = 0$ (monopole)	1	$+$	$-$	$n \geqslant 1, l = 0$	$D_g^{(0)}$
	ABM	H_g	$l = 2$ (quadrupole)	5	$+$	$-$	$n \geqslant 1, l = 2$	$D_g^{(2)}$
C_s	RBM	A'	$l = 0$	1	$+$	$+$		
	ABM	A', A''	$l = 0$	1	$+$	$+$		

[a]See text.
[b]Irrep is short for the irreducible representation.
[c]A + symbol (− symbol) indicates that a mode is Raman and/or infrared active (inactive).
[d]See text and Refs [19,20]. Since C_s clusters are anisotropic, there can be no matching Lamb mode.

for aluminum, which is fitted by the force-matching method [36]. Compared with experimental results, it can reproduce bulk phonon frequencies fairly well [36,37], which is essential for studying vibrational modes.

III. RESULTS AND DISCUSSION

A. Group theory analysis and normal modes

From symmetry considerations, one may conclude some general features of BMs. Consider a continuous sphere first. We focus on fundamental vibrational modes, and overtones are simply ignored. Phenomenologically, RBMs are monopolar modes of isotropic expansion and contraction with $D_g^{(0)}$ symmetry, while ABMs generate a quadrupolar transformation between the oblate and prolate spheroids with $D_g^{(2)}$ symmetry but not vice versa. Here l of an irreducible representation (irrep) $D_g^{(l)}$ is the angular momentum in the physical context.

Point groups of nanoclusters are all finite. Among them, the I_h group has the highest symmetry in three-dimensional space, which can embody both $l = 0$ (A_g) and $l = 2$ (H_g) multipolar modes. For amorphous clusters, the fivefold degeneracy would be lifted, and the quadrupole is split into combinations (i.e., direct products) of several irreps. For instance, the nondegenerate C_s group has only a single symmetry element, so that the reducible representation of a quadrupole is $3A' + 2A''$ [38]. Consequently, both A' and A'' modes are candidates for ABMs in this case. With detailed analysis, we can obtain all possible connections between BMs and groups, which is summarized in Table I.

Symmetry constraints determine the possible changes in particular GQs of nanoclusters. We must emphasize that group theory implies only symmetry. (i) It tells us nothing about addition information on shape variations, which is determined by actual configurations and materials. (ii) Also, it *never* ensures any mode with a certain symmetry will be a BM.

To remedy issue (i), we perform a conventional normal mode analysis by diagonalizing the dynamical matrix D_{ij}, which reads

$$D_{ij} = \frac{1}{m} \frac{\partial^2 U}{\partial \mathbf{r}_i \partial \mathbf{r}_j} \quad i, j = 1, 2, \ldots, N, \quad (10)$$

where U is the interatomic potential. Our results suggest, for I_h clusters, only RBM would cause the volume and surface area to change, but fluctuations in the volume may be subtler due to cancellations between different parts.

As for issue (ii), one must carefully check mode patterns. The presence of degeneracy, nevertheless, makes it harder to analyze since eigenvectors can be linearly combined in an infinite number of ways. Here we propose a recombination technique to resolve this issue and take I_h clusters as an illustration. Let $\mathbf{u}_s$, $s = 1, 2, \ldots, 5$, be five complete orthonormal eigenvectors of an ABM (H_g irrep). We can recombine them to maximize its radial component, namely,

$$\max_{c_s} \mathbf{u} \cdot \hat{\mathbf{r}} = \sum_{s=1}^{5} c_s \mathbf{u}_s \cdot \hat{\mathbf{r}} \quad (11)$$

$$\text{s.t.} \quad \sum_{s=1}^{5} c_s^2 = 1, \quad (12)$$

where $\hat{\mathbf{r}}$ is a radial unit vector. Equation (12) ensures the recombination ($\mathbf{u}$) is also a unit vector. By transforming $\{c_s\}$ to hyperspherical coordinates $(r, \phi_1, \ldots, \phi_4)$ and disregarding angular ranges, one could lift all constraints to obtain a global optimization, which has solutions forming a four-dimensional lattice. Basin hopping [39] is the most effective algorithm for this problem and converges after dozens of iterations.

As illustrated in Fig. 2, the recombined vector $\mathbf{u}$ [Fig. 2(a)] is projected onto a plane perpendicular to the principal axis
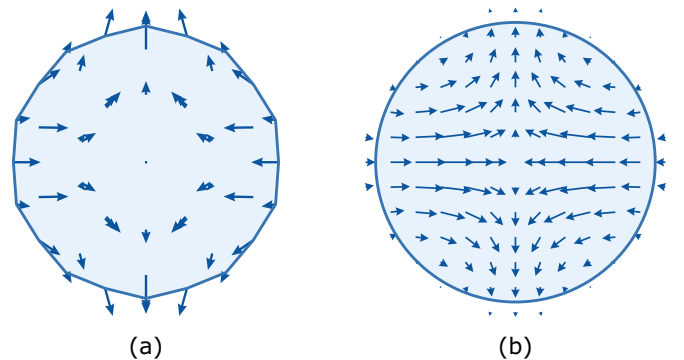

(a)   (b)

FIG. 2. Quadrupolar displacement fields of (a) the atomic and (b) continuous models; both are normalized to give unit length. Vibrational eigenvectors of an ABM are calculated by diagonalizing the dynamical matrix of Al_{55} and recombined to maximize the radial component. Arrows in (a) demonstrate the projected distribution of recombined vectors. Arrows in (b) refer to the continuous displacement field numerically calculated from Lamb's analytic results [19,21]. Both models give very similar mode patterns, which suggests the validity of CET at nanoscale.

TABLE II. Radial breathing modes.

Cluster	Mode ID[a]	Irrep	Frequency (THz)	Geometric quantities[b]								
				V_e	V_{ws}	V_h	S_e	S_h	$R_\alpha^{(s)}$	R_α	$e_{\alpha\beta}^{(s)}$	$e_{\alpha\beta}$
Al_{13}	$\mathcal{R}_{13}^a$	A_g	9.274	+	+	+	+	+	+	+		
	$\mathcal{R}_{55}^a$		5.687	+	+	+	+	+	+	+		
Al_{55}	$\mathcal{R}_{55}^b$	A_g	6.445	+	+	+	+	+	+	+		
	$\mathcal{R}_{55}^c$		11.87		+	−		+				
	$\mathcal{R}_{147}^a$		3.426	+	+	+	+	+	+	+		
	$\mathcal{R}_{147}^b$		4.460	+	+		+	+	+	−		
	$\mathcal{R}_{147}^c$		5.511	+	−	+	+	+	+			
Al_{147}	$\mathcal{R}_{147}^d$	A_g	7.549	+	+	+	+	+	+			
	$\mathcal{R}_{147}^e$		8.628	+	+	+	+	+	+			
	$\mathcal{R}_{147}^f$		10.09		+	−		+				
	$\mathcal{R}_{147}^g$		12.15		+	−		−				
	$\mathcal{R}_{43}^a$		2.026–2.449[c]	+			+					
	$\mathcal{R}_{43}^b$		3.358	+			+	+				
Al_{43}	$\mathcal{R}_{43}^c$	A'	5.589–6.049[c]	+	−	−	+	+	+(x)[d]		+(xy)[d]	
	$\mathcal{R}_{43}^d$		6.223	+	+	+	+	−				
	$\mathcal{R}_{43}^e$		6.536	+	+	+	+	+				

[a]Mode ID gives the name of each mode.

[b]Geometric quantities are defined in Sec. II. A + symbol denotes a clear signal, and a − symbol means a weak signal; otherwise, a blank cell implies the mode is undetectable.

[c]As peaks are broadened, shifted, and overlapped due to more profound anharmonicity in Al_{43}, some modes at very close frequencies are grouped together as a band of breathing modes.

[d]α, $\beta = x$, y, and z are the short, medium, and long axes of Al_{43}, respectively. Combinations such as $\alpha\beta = xy$ are planes defined by two axes.

z, which resembles the corresponding $m = 0$ displacement field [Fig. 2(b)] of a continuous elastic sphere. m is the projected angular momentum along the z axis. Our method, consequently, enables us to directly compare both models. Conversely, the widely known projection method, which projects atomic vibrational modes onto a continuous elastic displacement field, was found to be erroneous when applied to ABMs [17]. For isotropic clusters (e.g., Al_{55}), peaks resembling a H_g degenerate mode "smear" around the real one. For anisotropic clusters (e.g., Al_{43}), the degeneracy is partially lifted. In this situation, contributions from spherical and torsional modes would mix together [17]. Both drawbacks can be understood from issue (ii) mentioned earlier and will not emerge in our recombination technique.

Mackay icosahedron (I_h group) is a common quasicrystal packing structure of nanoparticles [40]. Suppose a Mackay cluster Al_N consists of $n \geqslant 1$ icosahedral shells, with $10n^2 + 2$ atoms in each shell. From group theory, one may deduce the times of occurrence of A_g and H_g irreps, respectively,

$$c(A_g) = \frac{1}{48}[4n^3 + 18n^2 + 20n + 3 - 3(-1)^n], \quad (13)$$

$$c(H_g) = \frac{1}{48}[20n^3 + 42n^2 + 28n + 3 - 3(-1)^n]. \quad (14)$$

By checking mode patterns, such as in Fig. 2(a), we found the numbers of RBMs and ABMs are

$$c(\text{RBM}) = c(A_g), \quad (15)$$

$$c(\text{ABM}) = 1 < c(H_g). \quad (16)$$

Our analysis is different from previous works [1,17], in which only one RBM per cluster was identified.

B. Breathing modes from MD simulations

In Tables II and III, we present BMs of those four clusters. Selected examples of PS are depicted in Fig. 3. Frequencies calculated by the MD and dynamical matrix agree fairly well since anharmonicity is weak at 100 K. The + symbol indicates a clear peak, where the signal-to-noise (SN) ratio is greater than 10; a − symbol means a faint signal with $0.1 < \text{SN ratio} \leqslant 10$; otherwise, a blank cell in Tables II and III implies the signal is imperceptible if SN ratio $\leqslant 0.1$ or even nonphysical. $\mathcal{R}_{43}^b$ in Table II and $\mathcal{A}_l$ in Table III are actually the same mode. Such a dual role reflects the amorphousness of Al_{43}, where an axial mode can also produce recognizable radial movements in *all* directions.

In practice, some GQs may be more efficient than others for given modes, which can be easily seen from Tables II and III. Notably, there is a qualitative difference between I_h and C_s clusters. For the former, V_{ws} and S_h are the best for RBMs, while unsorted $e_{\alpha\beta}$ is suitable for ABMs. However, for C_s clusters, ellipsoidal bounding V_e and S_e are better to identify RBMs, but sorted $R_\alpha^{(s)}$ and $e_{\alpha\beta}^{(s)}$ are the most effective to locate ABMs. We emphasize that sorted GQs are not valid for icosa-

TABLE III. Axial breathing modes. See the footnotes to Table II for additional details.

Cluster	Mode ID	Irrep	Frequency (THz)	Geometric quantities								
				V_e	V_{ws}	V_h	S_e	S_h	$R_\alpha^{(s)}$	R_α	$e_{\alpha\beta}^{(s)}$	$e_{\alpha\beta}$
Al_{13}	$\mathcal{A}_{13}$		5.576						−	+	+	+
Al_{55}	$\mathcal{A}_{55}$	H_g	2.528							+		+
Al_{147}	$\mathcal{A}_{147}$		1.117							+		+
	$\mathcal{A}_s$	A''	2.702						+(z)		+(zx)	
Al_{43}	$\mathcal{A}_m$	A'	2.863						+(y, z)		+(yz)	
	$\mathcal{A}_l$	A'	3.358	+			+	+	+(x)		+(xy)	

hedral clusters (Al_N, $N = 13, 55, 147$) since each of them has 12 equivalent directions, distributed isotropically. Thermal fluctuations will interrupt the sorting procedure (Sec. II) and generate nonphysical signals. Therefore, one must restrict the use of the sorted GQs (here referring to radii of gyration) to nonspherical systems.

C. The linear relationship

The most notable result of Lamb's analysis is the linear relationship between eigenfrequencies ν and the reciprocal of

FIG. 3. Selected power spectra of geometrical quantities for (a)–(c) Al_{13} and (d)–(f) Al_{55}. (a)–(c) compare the characteristics of three sets of geometric quantities (volume and surface, R_α, and $e_{\alpha\beta}^{(s)}$). Volume and surface in (a) clearly identify the RBM $\mathcal{R}_{13}^a$, while $e_{\alpha\beta}^{(s)}$ in (c) unambiguously pinpoints the ABM $\mathcal{A}_{13}$. Focusing on the RBM labeled as $\mathcal{R}_{55}^c$, (d)–(f) highlight the performance of three algorithms for volume. The ellipsoidal approximation V_e, oversimplified, fails to capture this mode. [Note that the miniature signal in (d) *alone* could not be *confidently* identified as a breathing mode.] The volume sum of Wigner-Seitz cells V_{ws} is the most efficient one, while convex bounding V_h is acceptable but not so satisfactory. (d), (e), and (f) exemplify peaks that are "imperceptible," clear (+), and weak (−), respectively.

the diameter $1/d$. Due to the uncertainty of nano-objects, the mathematical definition of the diameter d is not quite rigorous. Instead, we use Wigner-Seitz radii r_s of bulk aluminum to approximate cluster diameters [41],

$$r_s = \sqrt[3]{\frac{3}{4\pi\rho}}, \qquad (17)$$

$$d = 2r_s N^{1/3}, \qquad (18)$$

where ρ is the bulk density. For aluminum, $r_s = 1.095$ Å [42].

Figure 4 illustrates the frequency-diameter relationships. Clearly, for I_h clusters, the lowest frequencies of BMs [branches (b) and (c) in Fig. 4] scale *quasi*linearly with $1/d$. Similar results were confirmed both theoretically and experimentally in other metallic nanoclusters of a broader size range [1,3,18,23–25]. From underlying principles, we shall believe this linearity holds for larger aluminum clusters, as their cutoff wavelength is longer, which is essential to the continuous medium approximation.

The low-symmetry Al_{43} is an oblate spheroid; naturally, it may not match the predictions of Lamb's model. However, from Fig. 4, we can roughly conclude their frequencies are very close to two fundamental branches [i.e., Fig. 4, branches (b) and (c), BMs with the lowest frequencies] of I_h clusters. A comparative CET solution for an ellipsoid cannot be written in a closed form, and numerical methods are required. As a reference, Visscher *et al.* have developed a nice scheme based on the Hamilton's principle [43]. Such comparison, however, is beyond our scope.

D. Breakdown of continuous elastic theory

Apparently, for BMs with higher frequency, as shown in Fig. 4, the quasilinear relationship breaks down. One reason is the reduction of eigenmodes [2,17]. For instance, Al_N has only $3N - 6$ vibrational modes. As N decreases, most Lamb modes would be entirely eliminated, which is a characteristic feature of nanoclusters.

Despite the above facts, one may still suspect two branches of RBMs connected by dashed lines [Fig. 4, branches (d) and (e)] may be high-frequency $l = 0$ Lamb modes. A careful comparison of mode patterns, however, confirms they are spurious. Note that Lamb's model assumes spherical symmetry; the following discussions are focused on only I_h clusters.

The first disparity between CET and the atomic model is the occurrence of nonradial displacements. Such a property can be qualified by a normalized quantity called *radiality*,
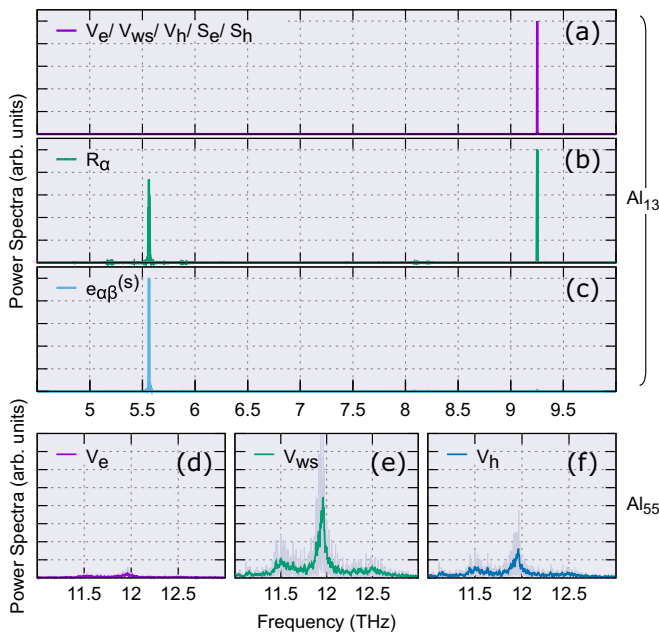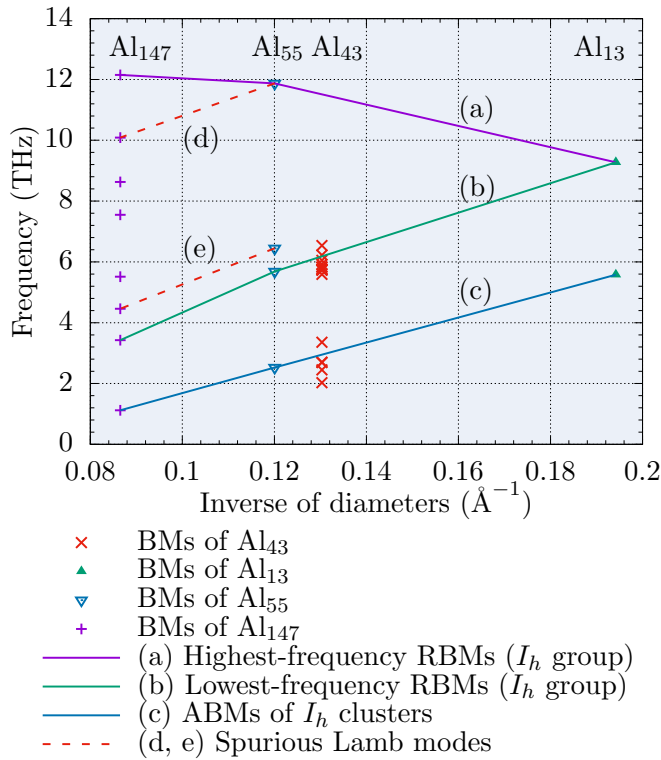
FIG. 4. The quasilinear relationship between BM frequencies ν and the inverse of the diameter $1/d$. Frequencies are calculated from MD simulations at 100 K, and diameters are approximated by Wigner-Seitz radii (see text). The two lower branches (b) and (c) are related to Lamb's fundamental $l = 0$ RBM and $l = 2$ ABM, respectively. Normal modes of (b) and (c) are in-phase vibrations, whereas others involve out-of-phase motions. Branches (d) and (e) are *spurious* Lamb modes since they seem to exhibit the same quasilinear behavior as (b) and (c). The detailed study rejects such likelihood since some of them have nonradial displacements or nonidentical outline shapes, conflicting with predictions of CET (Sec. III D). BMs of low-symmetry Al_{43} also stay close to Lamb's modes (b) and (c), even though Al_{43} is approximately ellipsoidal.

inspired by Henning *et al.* [16],

$$\delta_r = \sqrt{\frac{1}{N - N_e} \sum_{i=1;\, \mathbf{u}_i,\, \mathbf{r} \neq \mathbf{0}}^{N} |\hat{\mathbf{u}}_i \cdot \hat{\mathbf{r}}|^2} \in [0, 1]. \qquad (19)$$

$\hat{\mathbf{u}}_i$ is a unit vector along the displacement of the ith atom, and N_e is the number of atoms to be excluded, where either $\mathbf{u}_i$ or $\mathbf{r}$ vanishes. Within CET, $D_g^{(0)}$ symmetry permits only radial movements ($\delta_r = 1$), so that many authors have defined RBM as a *purely radial* mode [10,12,13]. We found two phenomena contrasting this definition. First, several T_{1u} *dipolar* modes of Al_{13} also have $\delta_r = 1$, but without any breathinglike feature at all. (Note that RBMs should have *even* parity.) Second, a few RBMs of Al_{147} bear $\delta_r < 1$; as shown in Fig. 6, atoms on the outermost edges have nonvanishing transverse shifts. Those shifts are caused by *local* symmetry breaking; namely, for each particular atom on the edge, its first-nearest neighbors distribute asymmetrically. Although branch (d) in Fig. 4 seems like a Lamb mode, the existence of tangential torsion under $\mathcal{R}_{147}^g$ (Table II) rules out such a possibility.
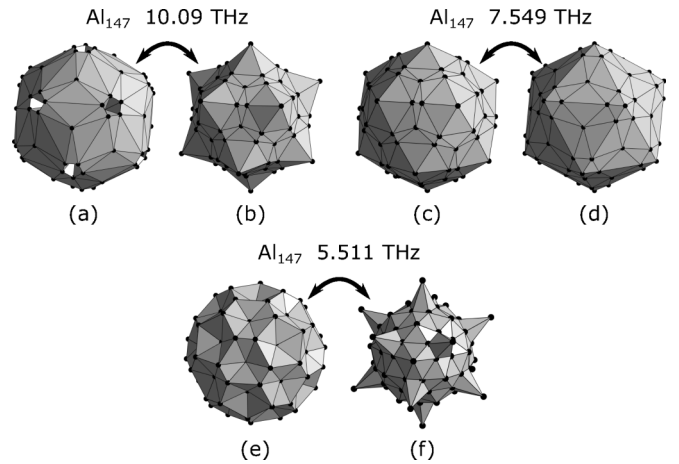

FIG. 5. Nonradial surface deformation caused by a few high-frequency RBMs of Al_{147}. Each mode makes the cluster transform between a pair of polyhedra. For example, $\mathcal{R}_{147}^f$ ($\nu = 10.09$THz) prompts Al_{147} to move back and forth between (a) and (b). For clarity, deformation is exaggerated, and polyhedra are scaled to the same size. As illustrated in each panel, nonradial motions of atoms on the edge distort surface-center hexagons from regular ones. This phenomenon contradicts Lamb's prediction, where RBMs produce purely radial vibrations. $\mathcal{R}_{147}^d$ is the only one which keeps the icosahedral outline unchanged, as in (c) and (d).

The second discrepancy with CET arises from surface mode patterns. From the similarity principle, two elastic spheres of different sizes under a RBM must have exactly the same outlines. Figure 6 depicts the shapes of Al_{55} and Al_{147} under selected RBMs, exaggerated for clarity. Indisputably, Figs. 6(a) and 6(e) or Figs 6(b) and 6(f) do not resemble each other; thus, branch (e) in Fig. 4 is also fictitious.
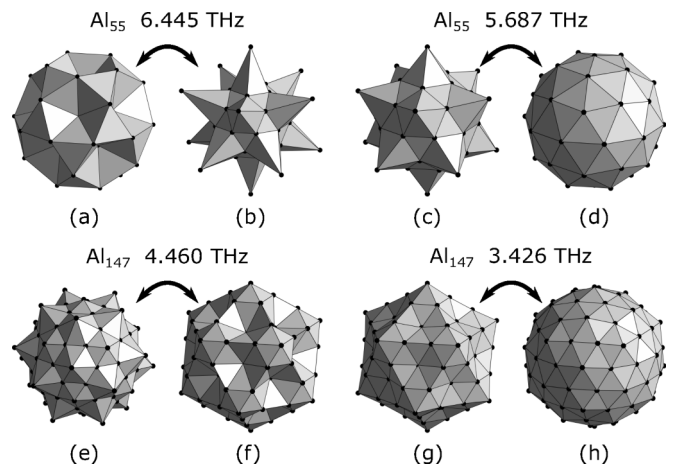

FIG. 6. Stellations induced by selected high-frequency RBMs of (a)–(d) Al_{55} and (e)–(h) Al_{147}. (a) [or (b)] and (e) [or (f)] are two modes connected by the dashed line in Fig. 4(e), while (c) [or (d)] and (g) [or (h)] represent the fundamental Lamb mode in Fig. 4(b). Two clusters under the same Lamb mode have very similar shapes, e.g., small stellated dodecahedra in (c) and (g), as well as spheres in (d) and (h). Because neither (a) and (e) nor (b) and (f) resemble each other, they do not belong to any Lamb mode.
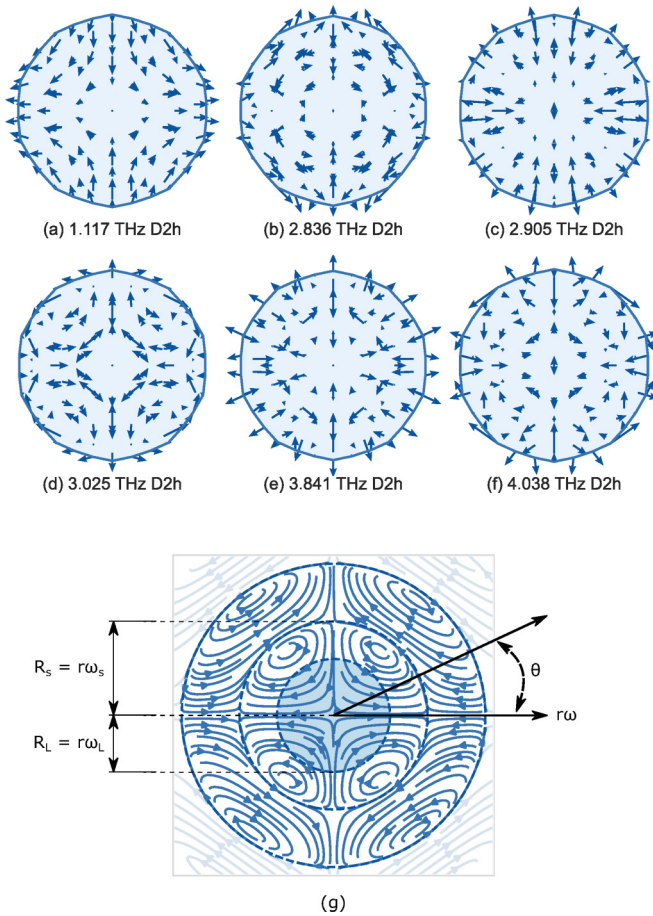
(a) 1.117 THz D2h   (b) 2.836 THz D2h   (c) 2.905 THz D2h

(d) 3.025 THz D2h   (e) 3.841 THz D2h   (f) 4.038 THz D2h

(g)

FIG. 7. (a)–(f) projected distributions of recombined displacements of H_g modes and (g) their continuous analogy derived from CET. (a)–(f) are calculated from the dynamical matrix of Al$_{147}$ and recombined with a method described in Sec. III A. (g) demonstrates a numerical solution to the quadrupolar mode of Lamb's model, plotted in scaled polar coordinates $(r\omega, \theta)$, where r is the radius of an elastic sphere and ω is the angular frequency. A low-frequency mode $(\omega = \omega_L)$ has a scaled radius $r\omega_L = R_L$, i.e., the innermost circle in (g), which has mode patterns similar to those of the ABM demonstrated in (a). When ω happens to reach ω_s and $r\omega_s = R_s$, there will be no radial displacement on the surface; thus, the elastic sphere exhibits only internal vortical twists, resembling the mode in (d). In addition, this form of vibration does not show any breathinglike pattern at all. As ω increases, patterns in (g) suggest both types would occur repeatedly. From (a)–(f), however, it is clear that most atomic quadrupolar modes cannot be explained by Lamb's theory.

So far, we have reached the conclusion that CET can reproduce displacement fields well for the lowest-frequency RBMs alone.

E. Predictions beyond continuous elastic theory

As already discussed in Sec. III A, for I_h clusters, we found all A_g modes are RBMs but only one ABM among several H_g modes. To demystify the inequality between H_g irreps and ABMs, Figs. 7(a)–7(f) depict projected distributions of selected H_g modes of Al$_{147}$, and Fig. 7(g) shows a displacement field derived from CET. The lowest-frequency ABM uniquely

exhibits breathinglike behavior. It confirms that *not* every mode with the required symmetry is a BM. As frequency increases, however, CET predicts the ABM will appear multiple times, except in the unlikely event that ω happens to have some critical values (e.g., ω_s in Fig. 7). Again, CET fails to accurately predict the atomic behavior at higher frequency, although a few modes such as that in Fig. 7(d) indeed exhibit the vortical patterns.

Out-of-phase vibrations could appear for high-frequency RBMs, which is very similar to optical phonons. Even though they are beyond the applicable scope of CET, Lamb's model still successfully predicts their existence [j_1 changes sign for $\xi > 4.5$ in Eq. (20); see below]. One question is, What do they *look like*? They were ignored in previous work [5,41], for their signals are weaker and do not preserve cluster shapes but bring about transformations between a pair of polyhedra. The latter phenomenon is very interesting. Most deformations are stellations of a regular icosahedron, including Kepler-Poinsot and excavated polyhedra, as depicted in Figs. 5 and 6. Forasmuch as the A_g irrep is totally symmetric, all such deformations maintain the full icosahedral symmetry (I_h point group). Remarkably, only the fundamental BMs [lines (b) and (c) in Fig. 4] of each cluster involve purely in-phase motions.

Signal damping makes it harder to detect out-of-phase RBMs experimentally, which can be deduced from CET as well. We start from the displacement field derived from Navier equations [44], given in spherical coordinates (r, θ, ϕ),

$$\mathbf{u}^{(l=0)} = A h j_1(hr)\hat{\mathbf{r}} = A h j_1(\xi)\hat{\mathbf{r}}, \tag{20}$$

where A is the amplitude, $h = \omega/v_l$ is the ratio of angular frequency ω to longitudinal sound speed v_l, $\xi = hr$ is a dimensionless quantity, j_n denotes spherical Bessel functions of the first kind, and $\hat{\mathbf{r}}$ is a radial unit vector. Higher-frequency RBMs induce smaller displacements on the surface and a more modest change in continuous RMSR $\mathscr{R}^c$,

$$\mathscr{R}^c = \sqrt{\int_\Omega r^2 \rho(r) d^3 V \Big/ \int_\Omega \rho(r) d^3 V}, \tag{21}$$

i.e., a continuous version of Eq. (7), since both $f(\nu)$ and $g(\nu)$ (defined below) decrease monotonically,

$$f(\nu) = \sup\{|j_1(hr)|, h \geqslant 2\pi\nu/v_l\}, \tag{22}$$

$$g(\nu) = \sup\{|\mathscr{R}^c(h)/\mathscr{R}^c(0) - 1|, h \geqslant 2\pi\nu/v_l\}. \tag{23}$$

Accordingly, signal intensities of V_h, S_h, V_e, and S_e would decrease as frequency increases; the same trend is shown in Table II.

IV. SUMMARY

To resolve ambiguous and erroneous interpretations of breathing modes, we proposed a more general and consistent definition based on geometric quantities and their power spectra. Our approach is capable of covering all types of BMs (radial and axial, in-phase and out-of-phase BMs) and practical for finite temperatures, regardless of cluster symmetries. By comparing BMs between nanoclusters and isotropic

elastic spheres of Lamb's model, we find that stellated geometry and tangential movements can be understood only at the atomic level, where continuous elastic theory breaks down. Also, a comprehensive study on the vibrational properties of additional spherical and nonspherical clusters is still highly desirable. Although the exact details of the vibrational properties, such as BM frequencies and nonradial surface deformation, are specific to aluminum clusters, our methodology remains general purpose and unrestricted by the system under study.

[1] H. E. Sauceda, D. Mongin, P. Maioli, A. Crut, M. Pellarin, N. Del Fatti, F. Vallée, and I. L. Garzón, J. Phys. Chem. C **116**, 25147 (2012).

[2] A. Tamura and T. Ichinokawa, J. Phys. C **16**, 4779 (1983).

[3] H. E. Sauceda and I. L. Garzón, Phys. Chem. Chem. Phys. **17**, 28054 (2015).

[4] A. Posada-Amarillas and I. L. Garzon, Phys. Rev. B **54**, 10362 (1996).

[5] E. Ghavanloo, S. A. Fazelzadeh, and H. Rafii-Tabar, Int. Mater. Rev. **60**, 312 (2015).

[6] A. Arbouet, N. Del Fatti, and F. Vallee, J. Chem. Phys. **124**, 144701 (2006).

[7] G. V. Hartland, Annu. Rev. Phys. Chem. **57**, 403 (2006).

[8] N. Del Fatti, C. Voisin, D. Christofilos, F. Vallée, and C. Flytzanis, J. Phys. Chem. A **104**, 4321 (2000).

[9] N. Del Fatti, C. Voisin, F. Chevy, F. Vallée, and C. Flytzanis, J. Chem. Phys. **110**, 11484 (1999).

[10] D. Polli, I. Lisiecki, H. Portalès, G. Cerullo, and M.-P. Pileni, ACS Nano **5**, 5785 (2011).

[11] T. Zhou, C. Xu, X. Zhang, C. Cheng, L. Chen, and Y. Xu, Acta Phys. Chim. Sin. **24**, 1579 (2008).

[12] H. Portales, L. Saviot, E. Duval, M. Fujii, S. Hayashi, N. Del Fatti, and F. Vallée, J. Chem. Phys. **115**, 3444 (2001).

[13] J. H. Hodak, A. Henglein, and G. V. Hartland, J. Chem. Phys. **111**, 8613 (1999).

[14] A. Olivetti, J. Barré, B. Marcos, F. Bouchet, and R. Kaiser, Phys. Rev. Lett. **103**, 224301 (2009).

[15] K. D. Sattler, *Handbook of Nanophysics: Nanoparticles and Quantum Dots* (CRC Press, Boca Raton, FL, 2016).

[16] C. Henning, K. Fujioka, P. Ludwig, A. Piel, A. Melzer, and M. Bonitz, Phys. Rev. Lett. **101**, 045002 (2008).

[17] N. Combe and L. Saviot, Phys. Rev. B **80**, 035411 (2009).

[18] J. G. Aguilar, A. Mañanes, F. Duque, M. J. López, M. P. Iñiguez, and J. A. Alonso, Int. J. Quantum Chem. **61**, 613 (1997).

[19] H. Lamb, Proc. London Math. Soc. **s1-13**, 189 (1881).

[20] H. Lamb, Proc. London Math. Soc. **s1-13**, 51 (1881).

[21] L. Saviot and D. B. Murray, Phys. Rev. B **72**, 205433 (2005).

[22] A. C. Erigen and E. S. Suhubi, *Elastodynamics*, Vol. 2, *Linear Theory* (Academic, New York, 1975).

[23] J. G. Aguilar, A. Mañanes, M. J. López, M. P. Iñiguez, and J. A. Alonso, Int. J. Quantum Chem. **56**, 589 (1995).

[24] F. Calvo, J. Phys. Chem. C **116**, 7607 (2012).

[25] F. Calvo, J. Phys. Chem. C **115**, 17730 (2011).

[26] N. R. Raravikar, P. Keblinski, A. M. Rao, M. S. Dresselhaus, L. S. Schadler, and P. M. Ajayan, Phys. Rev. B **66**, 235424 (2002).

[27] J. Kürti, G. Kresse, and H. Kuzmany, Phys. Rev. B **58**, R8869 (1998).

[28] M. Machón, S. Reich, H. Telg, J. Maultzsch, P. Ordejón, and C. Thomsen, Phys. Rev. B **71**, 035416 (2005).

[29] D. W. Lozier, Ann. Math. Artif. Intell. **38**, 105 (2003).

[30] B. Delaunay, S. Vide, A. Lamémoire, and V. De Georges, Classe Sci. Math. **6**, 793 (1934).

[31] D. Y. Sun and X. G. Gong, J. Phys.: Condens. Matter **14**, L487 (2002).

[32] M. Ji, D. Sun, and X. Gong, Sci. China Ser. A: Math. **47**, 92 (2004).

[33] A. Nordsieck, Math. Comput. **16**, 22 (1962).

[34] J. R. Beeler, *Radiation Effects Computer Experiments* (Elsevier, New York, 2012).

[35] D. J. Wales, J. P. K. Doye, A. Dullweber, M. P. Hodges, F. Y. Naumkin, F. Calvo, J. Hernández-Rojas, and T. F. Middleton, "The Cambridge cluster database," (2001) .

[36] F. Ercolessi and J. B. Adams, Europhys. Lett. **26**, 583 (1994).

[37] Y. Mishin, D. Farkas, M. J. Mehl, and D. A. Papaconstantopoulos, Phys. Rev. B **59**, 3393 (1999).

[38] A. Gelessus, W. Thiel, and W. Weber, J. Chem. Educ. **72**, 505 (1995).

[39] D. J. Wales and J. P. K. Doye, J. Phys. Chem. A **101**, 5111 (1997).

[40] A. L. Mackay, Acta Crystallogr. **15**, 916 (1962).

[41] M.-Y. Ng and Y.-C. Chang, J. Chem. Phys. **134**, 094116 (2011).

[42] P.-G. Reinhard and E. Suraud, in *Introduction to Cluster Dynamics* (Wiley, Grünstadt, Germany, 2008), pp. 259–266.

[43] W. M. Visscher, A. Migliori, T. M. Bell, and R. A. Reinert, J. Acoust. Soc. Am. **90**, 2154 (1991).

[44] W. Cheng, S.-F. Ren, and P. Y. Yu, Phys. Rev. B **71**, 174305 (2005).